# Comparison between the properties of polyamide 12 and glass bead filled polyamide 12 using the multi jet fusion printing process

**Heather J. O' Connor and Denis P. Dowling**

School of Mechanical and Materials Engineering, University College Dublin, Belfield, Dublin 4, Ireland

*** Correspondence:** Email: heather.oconnor@ucdconnect.ie

## Abstract

This study investigates the material and mechanical properties of both polyamide 12 (PA12) and reinforced glass bead PA12 composites, fabricated using a production scale additive manufacturing (AM) process. The printing studies were carried out using the production scale, Multi Jet Fusion powder bed fusion process. The study demonstrated that the chemical functionality and the thermal properties of the printed PA 12 parts and the glass bead composite, were similar. Almost identical infrared spectra were obtained demonstrating the same chemical functionality. Based on DSC measurements, the melting temperature was 184°C and 186°C and the associated cooling cycle temperature was 150°C and 146°C for the composite and the PA12 respectively. The percentage crystallinity of the glass bead composite was 24 %, compared with the 31% obtained for the PA12 only parts. Based on mechanical tests, the addition of glass beads increased the tensile and flexural modulus by 85% and 36% and lowered the tensile and flexural strength by 39% and 15% respectively. The effect of print orientation during the MJF process was evaluated based on porosity and mechanical performance. Using X-ray micro computed tomography, it was demonstrated that the porosity of the PA12 and composite parts were less than 1%. Polymer and composite parts printed in the ZYX orientation were found to exhibit both the lowest porosity and highest mechanical strengths.

**Keywords:**

Multi Jet Fusion; PA 12; Glass Bead Composite; Powder Bed Fusion; Production Scale

## 1. Introduction

Additive manufacturing (AM) fabricates parts, layer by layer from a computer aided design (CAD) and allows for complex geometries, freedom of design and mass customisation [1]. In manufacturing, AM is transitioning from primarily prototyping to end use parts. The term AM encompasses many techniques such as material extrusion, vat photopolymerization and powder bed fusion (PBF) processes [2].

PBF processes consist of a thin, well packed, layer of powder being spread out and selectively fused with energy or a binder. In comparison with material extrusion and vat photopolymerization, PBF techniques are now widely applied in the healthcare, aerospace, marine and automotive sectors due to the range of available materials [3]. A particular advantage of this technology is that part support is not required during printing. PBF techniques includes binder jetting, selective laser sintering (SLS), high speed sintering (HSS) and multi jet fusion (MJF). Binder Jetting involves a printhead that selectively dispenses liquid binders to adhere polymer powders, layer by layer [3]. SLS uses a $CO_2$ laser as the heat source to selectively melt the powders and fuse them. HSS uses inkjet deposition of a radiation absorbing material followed by IR irradiation of the entire build surface to fuse each layer [4]. Similarly, MJF deposits fusing and detailing agents to enhance the sintering of the particles under IR lamps.

The most recently developed of these techniques is the MJF process, by Hewlett-Packard. This technique selectively coats a thin layer of polymer powder with fusing and detailing agents (to absorb IR radiation and to block it, respectively), prior to passing planar IR lamps across the powder bed, promoting uniform fusion of the specimen layer. A fresh layer of powder is then spread out over the first layer and the process is repeated, building up the 3D part [5, 6]. Compared with other PBF polymer techniques, the technique offers advantages of high productivity and low cost per unit volume, in terms of energy and material consumption [3].

Polymer powders have been widely adopted for research and commercial applications due to their wide range of physiochemical and mechanical properties once printed [3]. The polymer powders utilised in PBF processes primarily consist of semi-crystalline thermoplastics (such as polyamides, polypropylene and polyethylene), but also include amorphous thermoplastics (such as polystyrene and polycarbonate) and thermoplastic elastomers [7]. Polyamide 12 (PA12) is a semi-crystalline polymer and one of the most widely used polymers for PBF techniques [8, 9]. Its melt temperature is significantly higher than its crystallisation temperature. This extended ‘sintering window’ allows the speed of crystallisation to be reduced, thus reducing the accumulation of residual stresses and distortions [10]. PA12 is reported to have outstanding impact resistance and the lowest moisture absorbance of all the polyamides. Common demanding applications include fuel lines, connectors, seals, and conveyor belts [11].

In comparison to metal, polymer powders are limited by their thermal stability and mechanical strength. Therefore, extensive research on polymer composite powders, designed to fabricate functional parts with tailored mechanical properties, has been performed and is still underway. The range of materials investigated to date for powder composite materials suitable for PBF processes extends from polymer blends [12-14], to the use of fibres and particles as reinforcements [15-18] to the use of nanofillers [19-22]. Greiner et al. [13], combined different weight ratios of polybutylene terephthalate (PBT) and polycarbonate (PC) into a powder for SLS by wet grinding. It was observed that the addition of PC allowed the fabrication of monolayers by SLS (PBT is otherwise non-printable) and an increase in PC saw a decrease in porosity and layer thickness. Wang et al. [18], fabricated polyetherketone (PEK) and glass bead filled PEK using high temperature laser sintering. The PEK parts had a 10% lower tensile strength than that of injection moulded PEK but higher hardness. The addition of glass beads was found to yield an increase in hardness and thermal stability [18]. Qi et al. [19], prepared polyamide 11 / barium titanate (PA11 / $BaTiO_3$) powder for SLS, combining the techniques of solid state shear milling, melt blending and cryogenic grinding. The resultant parts exhibited excellent thermal properties, high dimensional accuracy and favourable mechanical strength.

Glass additives are often used as fillers in thermoplastics because they increase load-bearing capability in the elastic deformation range [23]. In their spherical form, they are reported to allow for high packing fractions, enhanced flow characteristics, increased part isotropy and less warpage - therefore making them a common choice for reinforcement [24, 25]. In terms of mechanical performance, thermoplastic filled glass bead parts have been well characterised for SLS [24, 26-28]. Cano et al. [27] studied the influences of temperature and print orientation on the mechanical properties of PA12 and PA12 reinforced with glass beads, printed via SLS. They found the fracture behaviour of the PA12 composite was unaffected by the temperature or print orientation and that the fracture resistance of the composite was extremely poor in comparison to the PA12 polymer parts. Seltzer et al [26] evaluated the effect of water on PA12 and PA12 reinforced with glass beads, fabricated using SLS and demonstrated that it caused a deterioration in mechanical performance. Chung et al. [17] investigated SLS printed Nylon 11, reinforced with glass beads and observed that the tensile and compressive modulus increases, while the strain at break and yield decreases as a function of glass bead volume. Negi et al. [28] studied how the process parameters during SLS affected the mechanical properties of glass filled PA12 and Xu et al. [29] evaluated the compressive performance of lattice structures fabricated using glass filled PA12, fabricated using SLS.

Studies published to date on the MJF process are based on the use of PA12 powder [5, 28-31]. This paper presents, for the first time, a characterisation of PA12 glass bead MJF fabricated specimens in terms of their chemical, thermal and mechanical properties. This study also includes an evaluation of the effect of print orientation during printing, on the porosity and mechanical properties of the resulting parts.

## 2. Experimental Methods

Polyamide 12 (PA12) and polyamide 12 reinforced with glass beads (PA12GB) test specimens were fabricated using a HP Jet Fusion 3D 4200 printer. This printer offers four printing regimes called balanced, mechanical, fast and cosmetic, which are selected depending on the print requirements. All parts in this study were printed using the balanced mode, which is reported to give both good mechanical performance and dimensional accuracy [30]. Each layer had a height of 80 µm and a printing time of approximately 10.5 seconds. The process consisted of one rolling step of the powder, followed by two fusing steps (Figure 1). The fusing and detailing agents were applied as described earlier in the introduction section; they are subsequently exposed to infrared planar lamps to facilitate selective sintering. This process was then repeated. The printed parts were positioned 10 – 15 mm apart, as shown also in Figure 2. They were then allowed to cool overnight, before being unpacked.

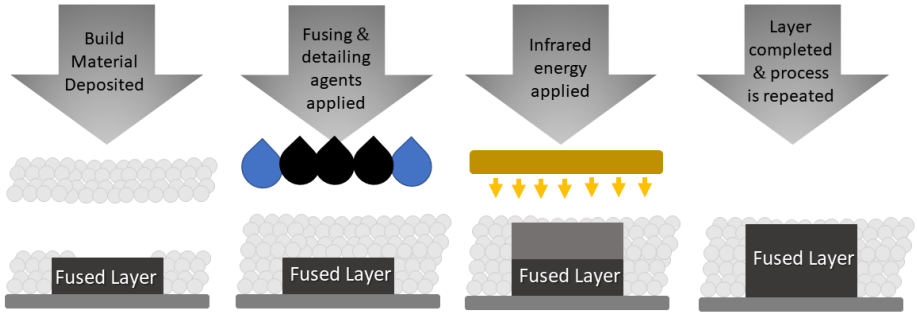


Figure 1: Schematic of the MJF printing process.

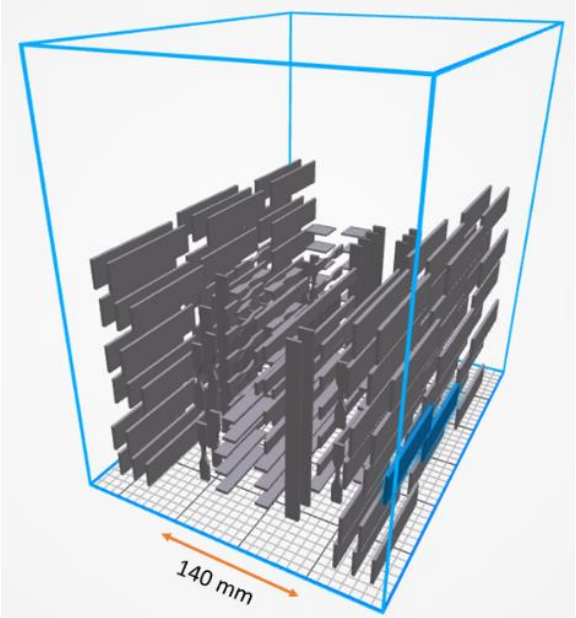


Figure 2: Schematic of the positioning of test parts on the build plate, note the different X, Y, Z orientations of the test specimens.

The powders used in this study were HP 3D High Reusability PA 12 and HP 3D High Reusability PA 12 Glass Beads. The powder characteristics are given in Table 1. As recommended by the manufacturer, the parts were fabricated using a 20:80 ratio of new to recycled powder using the HP 3D High Reusability PA12 and a 30:70 ratio of new to recycled powder using the using HP 3D High Reusability PA12 Glass Beads.

Table 1: Properties of the PA12 and PA12 glass bead powders [31, 32]

| | **Particle Size (μm)** | **Powder melting point (DSC)** | **Bulk Density g/cm$^3$** |
|---|---|---|---|
| **PA12 powder** | 60 | 187° C | 0.425 |
| **PA12 GB - 40% vol glass bead filled powder** | 58 | 186° C | 0.480 |

### *2.1 Print characterisation*

The PA12GB and PA12 specimen were characterised in terms of physical, chemical and mechanical properties and directly compared. Coupons with the dimensions of 2 × 25 × 25 cm were fabricated for characterisation. The loosely bound powder was removed using a Guyson Euroblast 6 blasting cabinet and glass beads (55 – 90 μm, Honite 18). The mass was obtained using a Sartorios MC1 Analytic AC 210 S balance and the part dimensions were measured using a digital vernier callipers, Digi Plus-Line – Vogel Germany GmbH & Co.KG. The results of which are given in Table 2.

Table 2: Mass and dimensions of PA12 and PA12GB fabricated coupons.

| **Material** | **Thickness (mm)** | **Length (mm)** | **Breadth (mm)** | **Weight (g)** |
|---|---|---|---|---|
| PA12 | 2.08 ± 0.03 | 24.95 ± 0.08 | 24.98 ± 0.11 | 1.24 ± 0.01 |
| PA12GB | 1.94 ± 0.01 | 24.87 ± 0.04 | 24.85 ± 0.03 | 1.51 ± 0.01 |

The morphology of the PA12 and the PA12 composite were compared using optical microscopy using an Olympus Gx51 Inverted Metallurgical Microscope and by scanning electron microscopy (SEM) on a Tabletop Hitachi TM4000 plus. Prior to optical examination, a thin conductive gold coating was applied by sputtering. The surface roughness of both materials was quantified and compared using an NP Flex Optical Profilometer, in vertical scanning interferometry (VSI) mode. The chemical and thermal properties of both the PA12 and PA12 composite were compared using attenuated total reflection infrared spectroscopy (ATR FT-IR) and differential scanning calorimetry (DSC). A Nicolet iS50 FTIR Spectrometer with a diamond ATR was used to obtain the FT-IR spectra, wavenumber range:

8000 - 650 $cm^{-1}$. The diamond crystal enables a depth of about 3 µm from the surface to be characterised. The specimens were freshly cut from the centre prior to scanning to avoid contamination. The DSC measurements were carried out using a Netzsch DSC214 system, with a heating rate of 10 K $min^{-1}$ under nitrogen. The glass transition temperature was evaluated according to the half-step method (DIN 51007). The percentage crystallinity ($X_m$) was calculated using Equation 1, where the enthalpy of fusion ($\Delta H_m$) was obtained from integrating the melting peak area using Proteus evaluation software and the heat of fusion of 100% crystalline PA12, $\Delta H_m^0$, was taken as 209.3 J $g^{-1}$ [10, 33].

$$X_m = \frac{\Delta H_m}{\Delta H_m^0} \times 100 \qquad \text{Equation 1}$$

*2.2 Mechanical performance*

In this study, the mechanical properties of the PA12GB were evaluated compared to the mechanical properties of the PA12 specimen. The PA12GB was evaluated in terms of tensile and flexural properties, looking at three build orientations XYZ, YZX and ZYX, simplified to X, Y and Z from here on, Figure 3. All mechanical testing was performed using a Zwick Roell z005 mechanical tester. The tensile tests were performed according to ASTM D 638 [34] with a 10 kN load cell, a video extensometer and a crosshead speed of 1 mm / min. Manual wedge grips and a pre-load of 0.1N was used and. A total of 10 specimens (type V) were tested at each print orientation. Flexural tests were performed on parts with the dimensions of 70 × 12.7 × 3.2 mm, with a preload of 1 N and a crosshead speed of 2 mm / minute, as per ASTM D 790 [35]. Specimens were tested to maximum deflection of 12 mm. A total of 10 samples were tested per print orientation. After mechanical testing, SEM (TM-2000 Hitachi) was used to examine the fractured samples.

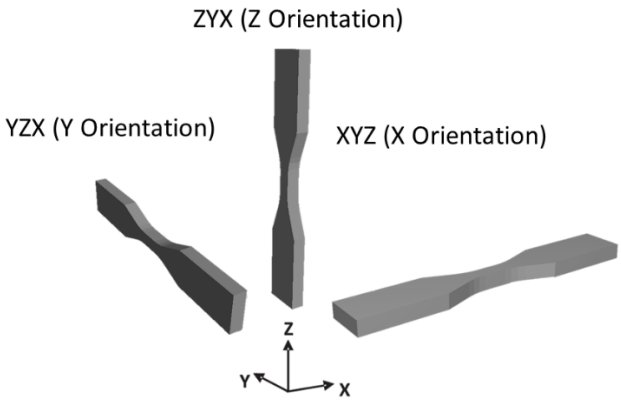


Figure 3: Schematic of type V dog bones from ASTM D638 in three build orientation axes - according to ISO/ASTM 52921

### *2.3 Porosity evaluation*

X-ray micro Computed Tomography (μCT) was used to calculate porosity. In the case of both the PA12 and PA12GB fabricated parts, a sample coupon of 10 × 13 × 3.2 mm was cut from the centre of a 175 × 13 × 3.2 mm bar (in triplicate) for each of the X, Y and Z orientations. The coupons were stacked in triplicate and mounted in Styrofoam. A maximum X-ray energy of 70 kV and 150 μA was used to scan each stack on a GE Nanotom m X-ray μCT scanner (GE Sensing & Inspection Technologies GmbH, Wunstorf, Germany). A total of 1200 projection images were acquired during a 9-minute scan with a resolution of 7 μm. The projection images were reconstructed to produce volumetric data using the software datos|rec (GE Sensing & Inspection Technologies GmbH, Wunstorf, Germany). The μCT volumes were then visualised using VG StudioMAX® 3.1.2. The 3D volumes were separated into low density (air) and high density (polymer and composite). Using the surface determination function, the percentage volume of the air present (the porosity), was calculated.

## 3. Results and discussion

### *3.1 Print characterisation*

The surface morphology of the PA12 and the PA12GB coupons was examined using optical microscopy. Prior to examination, the coupons were glass-bead blasted, as described in section 2, to remove loose powder and sputtered with a thin layer of gold to better visualise the surface. Figures 4 and 5 compare the morphologies of the PA12 and the PA12 composite. To quantify the surface roughness, two roughness parameters were used, the arithmetic mean height roughness $S_a$, and the root mean square height roughness $S_q$. The $S_a$ quantifies the deviations in height of the surface points in relation to the mean reference plane and the $S_q$ parameter determines the quadratic height of the measured surface. The glass bead composite has a significantly higher surface roughness ($S_a$) compared with that of the PA12 polymer, as detailed in Table 3. It was also observed for both the polymer and composite sample, that surfaces facing towards the build plate had a lower surface roughness, than that facing upwards. A possible explanation for this is that there may be some diffusion of the polymer during the sintering process, thus filling in voids towards the base of the part.

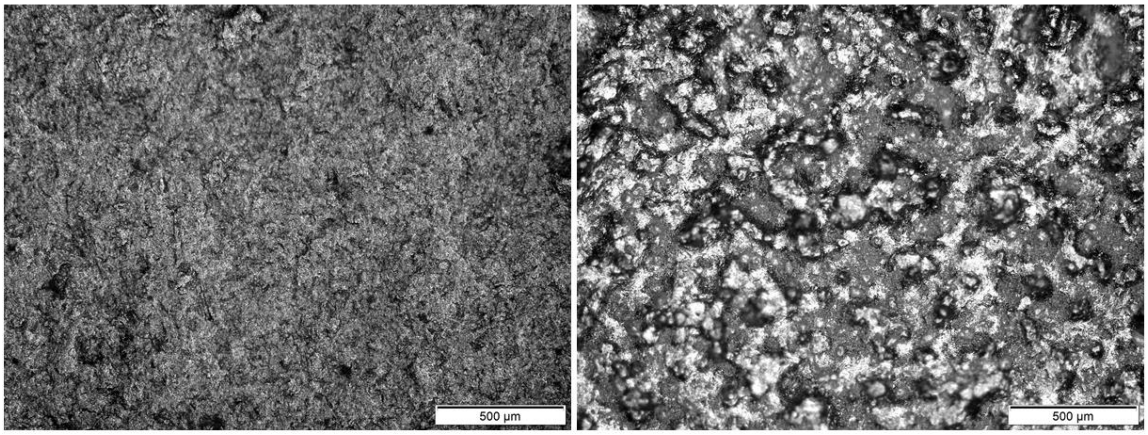


Figure 4: Optical microscopy comparison of the top surface morphology of the PA12 (left) and the PA12GB (right) printed coupons, obtained after glass bead blasting. Note the clearly visible glass beads in the composite surface. (scale 500 µm)

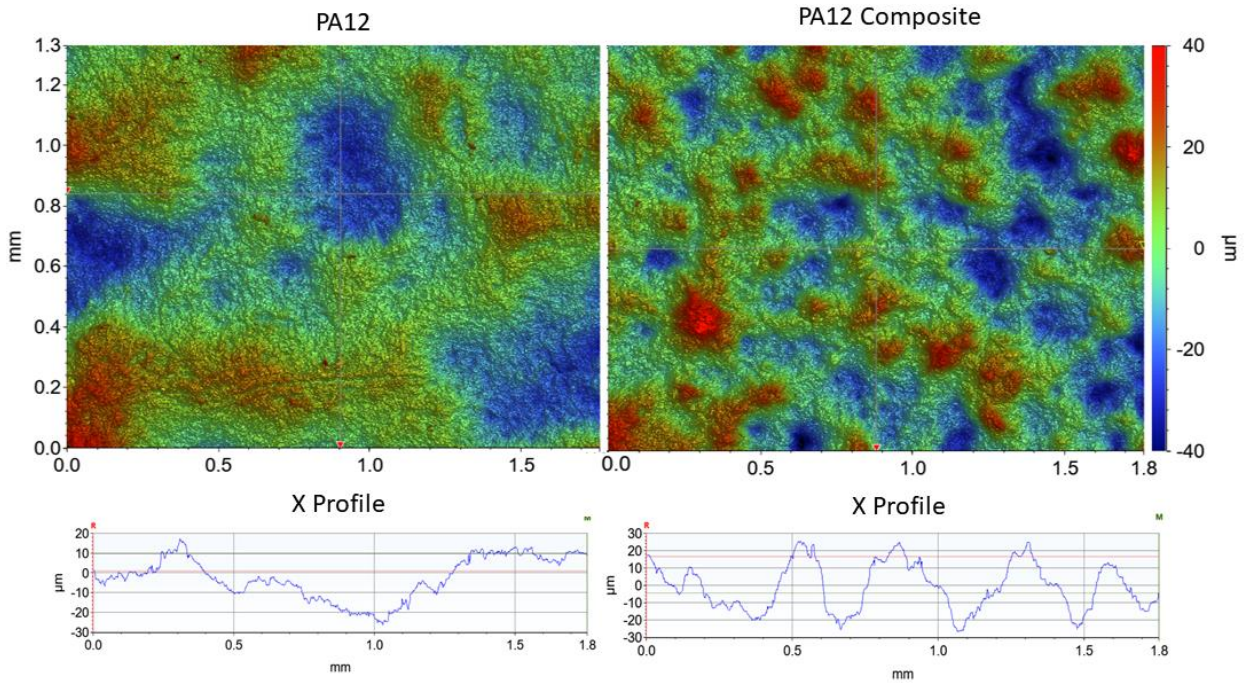


Figure 5: Optical profilometer comparison of the roughness scan of the PA12 and the PA12 composite surfaces after glass bead blasting (top images). Typical line scans demonstrating the enhanced roughness of the composite surface (bottom images).

Table 3: Roughness measurements of PA12 and PA12 composite parts.

| | $S_a$ | $S_q$ |
|---|---|---|
| PA12GB Top | 11.40 ± 1.46 | 14.21 ± 1.76 |
| PA12GB Bottom | 8.63 ± 0.12 | 11.08 ± 0.13 |
| | | |
| PA12 Top | 8.30 ± 0.12 | 10.31 ± 0.13 |
| PA12 Bottom | 4.12 ± 0.32 | 5.26 ± 0.28 |

During the powder bed fusion process, the recycling of the powder is extremely important, as it is key for both the process cost, as well as its sustainability. As mentioned in section 2, the parts were fabricated using a 20:80 ratio of new to recycled powder for the polymer only print and a 30:70 ratio of new to recycled powder for the composite print. These are extremely high ratios of recycled powder in comparison to traditional PBF methods. The recyclability of these powders is related to their molecular properties, such as their functional groups. FTIR was used to compare the functionality of the two printed parts. It was found that both powder materials when printed, exhibited FTIR spectra (Figure 6) which are very similar to that reported in the literature [36-38]. Table 4 details the main peak assignments, obtained for the MJF PA12 and PA12GB. Of particular interest are the frequencies sensitive to degradation, such as the N-H stretching vibration at 3298 $cm^{-1}$, the C=O stretching at about 1638 $cm^{-1}$ and the C-N stretching / N-H bending at 1544 $cm^{-1}$ [39]. No significant changes were observed for these frequencies, indicating high amide functionality of the printed parts.

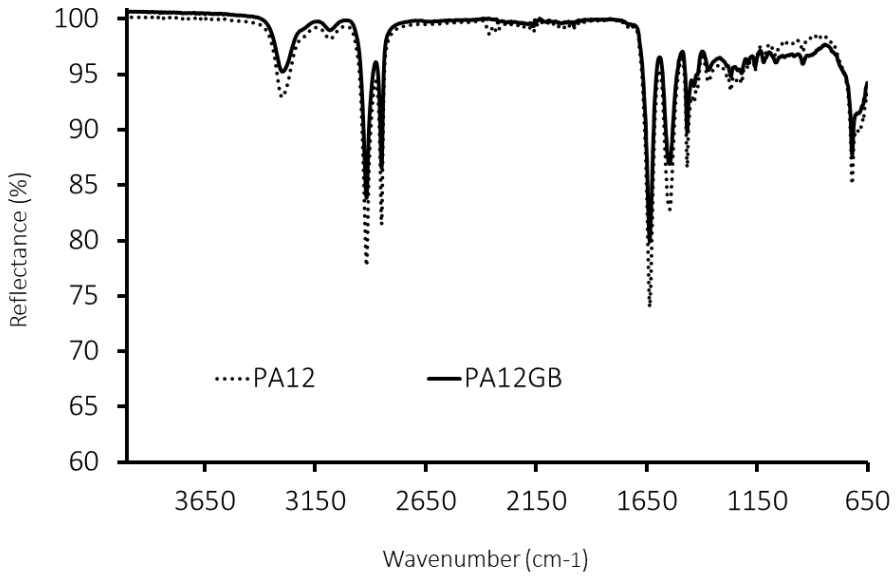


Figure 6: ATR infrared spectra of PA12 (dotted) and PA12GB (solid line), typical of PA12 printed from reused powder.

Table 4: Infrared peak assignments for Figure 6

| Vibrational frequency (cm-1) | Peak assignments |
|---|---|
| 3298 | N-H stretching |
| 3092 | Fermi resonance of the ν(N-H) stretching |
| 2918 | $CH_2$ asymmetric stretching |
| 2850 | $CH_2$ symmetric stretching |
| 1638 | Amide I, C=O stretching |
| 1544 | Amide II, C-N stretching & N-H bending |
| 1463 | $CH_2$ reference band |
| 1368 | CH bend, CH2 twisting |
| 1269 | Amide III, C-N stretching + C=O in-plane bending |
| 944 | CONH in plane |
| 718 | $CH_2$ rocking |

The thermal properties of the PA12 and PA12GB are compared in Table 5. This provides details on the glass transition temperature, their melting and cooling temperatures along with the percentage crystallinity. The results obtained for the PA12 specimen corresponds well with the thermal properties of SLS fabricated PA12 parts, reported in the literature [10, 40]. The PA12 composite parts saw minor differences in thermal properties, including a lower average glass transition temperature of approximately 4℃, a lower melt temperature of 2°C and a lower sintering window (metastable area between two phases) of 6℃. A 7% reduction in crystallinity is observed for the PA12 composite compared with that obtained for the polymer. A possible explanation for this, is that the incorporation of the glass beads induces heterogeneous nucleation, which would be detrimental to the polymer crystallinity.

DSC thermograms of PA12 and PA12GB are stacked in Figure 7, which exhibits both the glass transition temperatures as well as the first heating and cooling cycles (10 k/ $min^{-1}$). The glass transition temperature of the PA12 is higher than that obtained for the composite and a more noticeable step change in the thermogram is observed, probably associated with the higher concentration of PA12 polymer. Both PA12 and the PA12 composite yielded thermograms with a single, broad endotherm centred around 183 – 186 ℃, suggesting complete sintering of the powder during the MJF process, as a double-endotherm pattern, would be representative of incomplete sintering as often reported for SLS printed polymers [41].

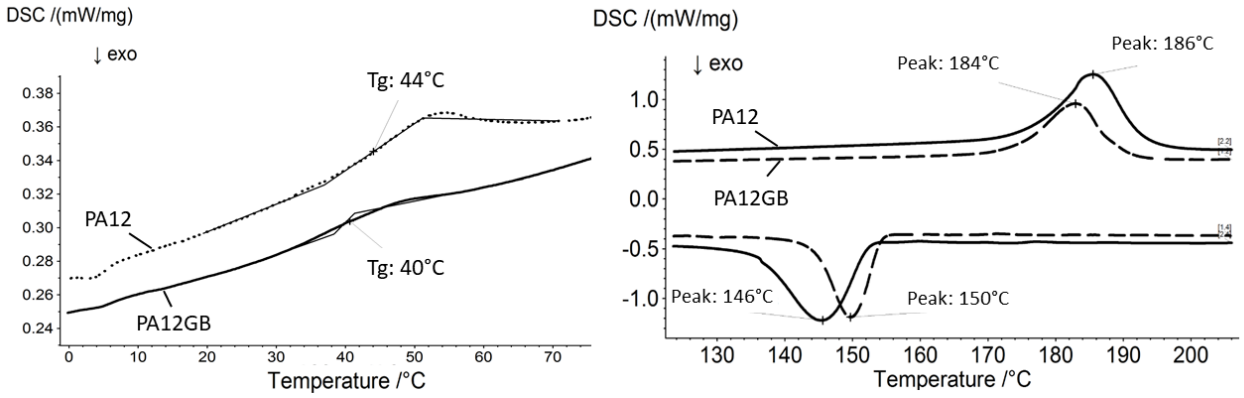


Figure 7: Stacked DSC thermograms comparing the glass transition temperature of PA12 and PA12GB (left) and the first heating and cooling cycle of both materials (right).

Table 5: A comparison of thermal properties of PA12 and PA12GB, where $T_g$ is the glass transition, $T_m$ is the melting temperature, $\Delta H_m$ melting enthalpy, $X_m$ percentage crystallinity, $T_c$ crystallisation temperature, $\Delta H_c$ crystallisation enthalpy, $X_c$ percentage crystallinity upon cooling.

| **Sample** | **Heating** | | | | **Cooling** | | |
|---|---|---|---|---|---|---|---|
| | $T_g$ (°C) | $T_m$ (°C) | $\Delta H_m$ (J/g) | $X_m$ (%) | $T_c$ (°C) | $\Delta H_c$ (J/g) | $X_c$ (%) |
| PA12 | 44 | 186 | 65 | 31 | 146 | 55 | 26 |
| PA12GB | 40 | 184 | 51 | 24 | 150 | 37 | 18 |

### *3.2 Mechanical performance*

The mechanical performance of the PA12 composite parts was evaluated in terms of tensile and flexural strength and compared to the PA12. To investigate the isotropy of the parts, the three build orientations detailed earlier, were investigated. The results of which are detailed in Table 6. The average tensile strength of the PA12 composite is 31 MPa, with a tensile modulus of 2276 MPa and an elongation at break of 6.1% and exhibited isotropic behaviour in terms of tensile strength.

The fracture surface of the PA12 composite at the tensile failure was observed using SEM. The failure mode was primarily ductile, with some areas of brittle failure. The two micrographs shown in Figure 9 provide examples of these two types of failure mode. By comparison, the failure mode of the PA12 tensile parts was primarily ductile. As observed in Figure 9, there appeared to be poor adhesion between the glass spheres and the polymer matrix. This is based on observing both holes left in the polymer matrix, where the spheres have dislodged as well as what visually appears to be relatively poor polymer to glass sphere bonding. Previous authors have highlighted the importance of a strong bond strength between the polymer and the glass, in order to achieve optimal mechanical performance [24, 27].

Table 6: Average tensile results, giving strength ($\sigma_{max}$), tensile modulus ($E_t$), and elongation at break ($\varepsilon_b$) of PA12 Composite and PA12.

| **Material / orientation** | **$\sigma_{max}$ (Tensile Strength)** | **$E_t$ (Tensile Modulus)** | **$\varepsilon_b$ (Elongation at Break)** |
|---|---|---|---|
| | MPa | MPa | % |
| PA12GB / X | 31 ± 0.8 | 2198 ± 175 | 5.9 ± 0.6 |
| PA12GB / Y | 31 ± 1.0 | 2332 ± 271 | 5.9 ± 0.9 |
| PA12GB / Z | 30 ± 0.9 | 2299 ± 226 | 6.5 ± 0.8 |
| PA12 / X | 47 ± 0.9 | 1242 ± 28 | 19 ± 2.8 |
| PA12 / Y | 48 ± 0.8 | 1147 ± 40 | 27 ± 1.2 |
| PA12 / Z | 49 ± 0.6 | 1246 ± 37 | 16 ± 1.9 |

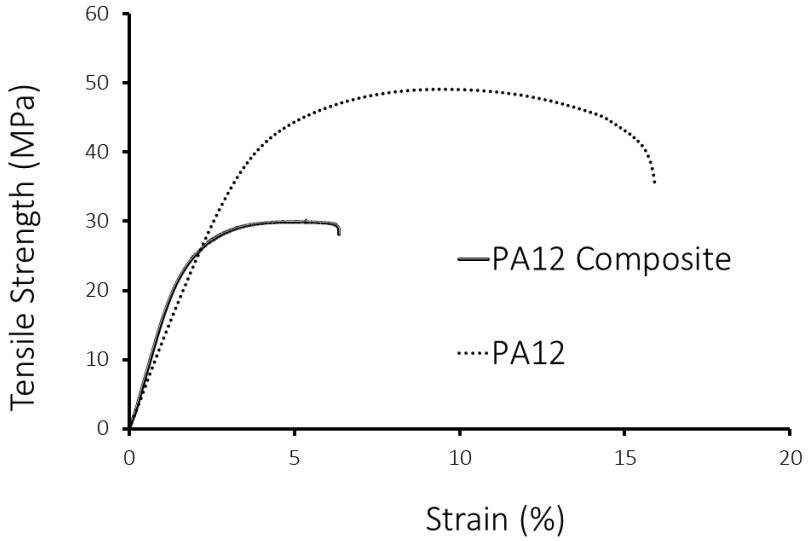


Figure 8: Tensile stress strain curves comparing the PA12 and PA12 glass bead composite (printed in the Z direction)

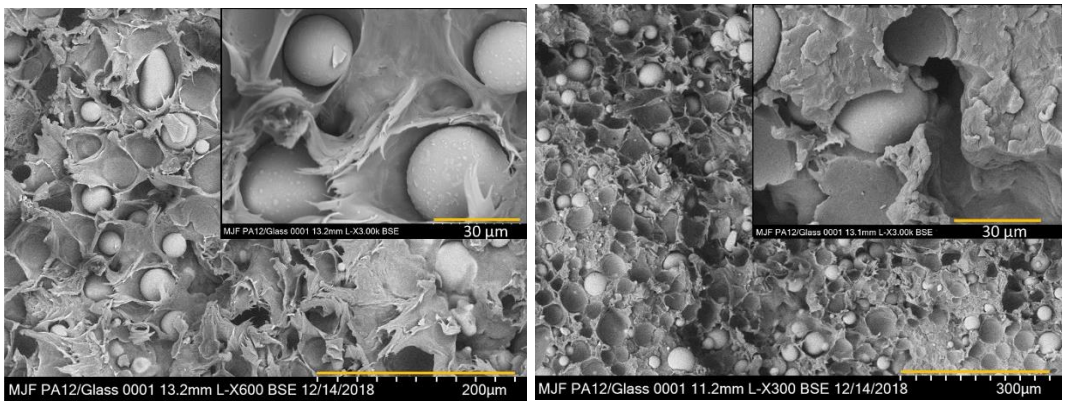


Figure 9: Micrographs of the fractured surface of PA12 composite after tensile failure demonstrating (left), ductile failure and (right), brittle failure modes.

Table 7 presents the results of the flexural strength examination of the printed PA12 composite along with those for PA12. In contrast to the tensile results, the part orientation during the printing process

appears to have some influence the flexural strength of the PA12 composite. The X, Y and Z orientation of the PA12GB have strengths of 50, 57 and 59 MPa and a flexural modulus of 1796, 2296 and 2292 MPa respectively. Figure 10 gives an example of a typical stress strain curve for both the PA12 composite and PA12, printed in the Z orientation. Similar to the tensile results, the composite exhibits a lower strength and higher modulus. Interestingly, in the case of the glass bead composite, the specimens fabricated in the X orientation did not rupture at max deflection, while 60 % of those printed in the Y orientation and 80% of those printed in the Z orientation ruptured. This suggests the part became more brittle when printed in the Y and Z orientation. In contrast, the PA12 parts experienced no failure during flexural testing. The addition of the glass beads increases the flexural modulus by 36 % while the flexural strength is lowered. The primary flexural failure mode was brittle, an example of which is given in Figure 11. Note what appears to be again, poor adhesion between the glass spheres and the polymer matrix, based on the smooth surface morphology of the glass beads [42].

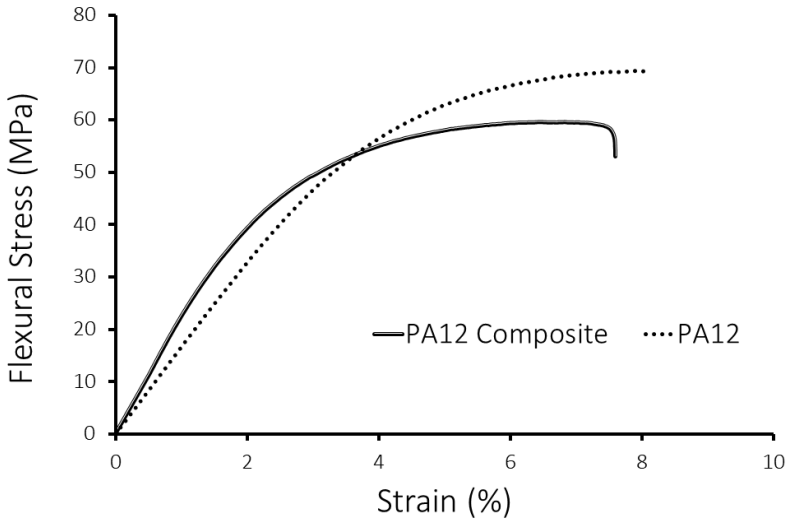


Figure 10: Flexural stress strain curves comparing the PA12 and PA12 glass bead composite (printed in the Z direction)

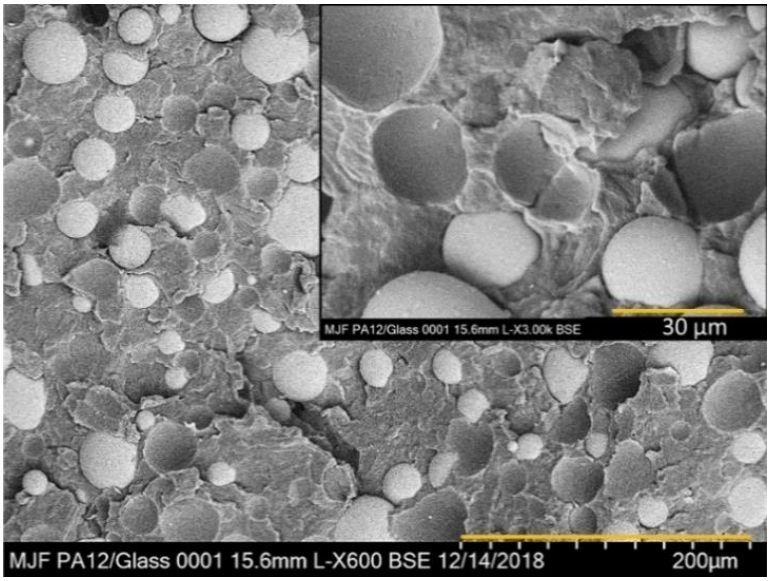


Figure 11: A micrograph of the typical flexural failure of the PA12GB specimen, exhibiting brittle failure.

Table 7: Average flexural results, giving the Flexural Stress ($\sigma_f$) and modulus ($E_f$) of PA12GB and comparing them to neat PA12

| **Material / orientation** | **$\sigma_f$ (Flexural Stress)** | **$E_f$ (Flexural Modulus)** |
|---|---|---|
| | MPa | MPa |
| PA12GB / X | 50 ± 2.0 | 1796 ± 73 |
| PA12GB / Y | 57 ± 1.4 | 2296 ± 97 |
| PA12GB / Z | 59 ± 1.4 | 2292 ± 144 |
| PA12 / X | 50 ± 0.9 | 1146 ± 51 |
| PA12 / Y | 66 ± 0.5 | 1567 ± 36 |
| PA12 / Z | 70 ± 0.7 | 1687 ± 12 |

Polyamide reinforced with glass beads is a popular choice of material for similar PBF processes, such as SLS. The tensile properties of the PA12GB powder used in this study are therefore benchmarked against literature values for two polyamide glass bead SLS powders. Due to variables in process parameters and type of PBF process used, a fully quantitative, direct comparison is difficult to make. However, based on this comparison with the literature values, it is clear that PA12GB parts printed using the production scale MJF™ process exhibit a mechanical performance comparable with those obtained using SLS. Note that the porosity of the PA12GB parts are significantly lower than for those reported for parts printed using the SLS technique, this will be discussed in more detail in the next section.

Table 8: A comparison of the tensile properties of PA12 powders, reinforced with glass beads, fabricated by powder bed fusion processes. Where $\sigma_{Max}$ is the maximum tensile strength, Et is the tensile modulus and εb is the percentage elongation at break.

| **Powder Name** | **PBF Process** | **Glass Beads (%)** | **Porosity (%)** | **$\sigma_{Max}$ (MPa)** | **$E_t$ (Mpa)** | **$\varepsilon_b$ (%)** |
|---|---|---|---|---|---|---|
| PA3200 (EOS) **[27]** | SLS | 40 | 2.8 | 29 | 2430 | 15 |
| Duraform GF (3-D Systems) **[26]** | SLS | 43 | 14.6 | 26 | 2910 | 3 |
| HP 3D High Reusability PA12 Glass Beads (HP) | MJF | 40 | < 1 | 31 | 2332 | 6 |

### *3.3 Porosity evaluation*

It is reported that SLS printed parts typically exhibit porosity values between 3 – 6% [43]. Investigations of the porosity of MJF printed parts, have to-date been based on optical microscopy using fractography analysis [44] as well as cross sectional analysis [6, 41]. Craft et al. [41], noted that almost complete sintering occurred in the MJF fabricated PA12 specimens, with only a few circular pores in the range of 50 μm pores observed. Table 9 details the porosity of the PA12 and PA12GB printed parts obtained using the X-ray micro Computed Tomography (μCT) technique, which provides a more quantitative evaluation of porosity. All specimens, with and without glass beads, printed in each orientation were found to have less than 1% porosity. This is considerably lower than typical SLS and it is thought to be a result of the combination of the fusing agent used to coat the polymer powder and the use of planar IR lamps overall gives a more heterogeneous layer upon sintering.

As demonstrated in Table 9, parts printed in the Z direction exhibit lower porosity, than those printed in the X and Y direction. Figure 12, on the left exhibits a 2D image of PA12 and on the right, its composite, taken from a CT scan using VG studios Max software. The images exhibit how the surface determination function, allows the porosity to calculated as a percentage volume of the 3D scan.

Table 9: Percentage porosity calculated from CT scans.

| **Material** | **Porosity of part orientation (%)** | | |
|---|---|---|---|
| | X | Y | Z |
| PA12 | 0.49 ± 0.09 | 0.66 ± 0.03 | 0.15 ± 0.05 |
| PA12GB | 0.98 ± 0.14 | 0.38 ± 0.04 | 0.27 ± 0.03 |

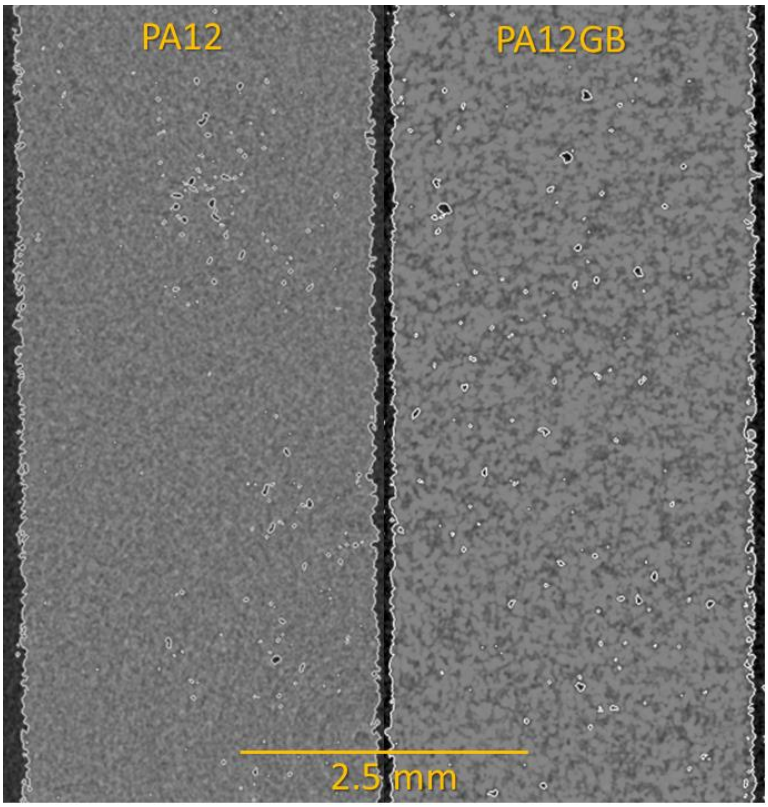


Figure 12: 2D image from CT scan of PA12 and PA12 GB printed in X orientation, exhibiting porosity (darker regions circled) using VG studios Max software.

As previously discussed in Table 7, the flexural properties of both the PA12 and PA12GB appear to be influenced by print orientation. In both cases the flexural strength increases from X < Y < Z. The porosity of the parts changes with print orientation. In the case of the PA12GB, as the flexural strength increases, the part porosity decreases. This is illustrated in Figure 13. This is also somewhat the case with the PA12 fabricated parts, except for the percentage porosity calculated for the Y orientation, which does not follow this trend and increases slightly, as illustrated in Figure 14. This is likely due to other factors, such as build position having an affect on the flexural strength.

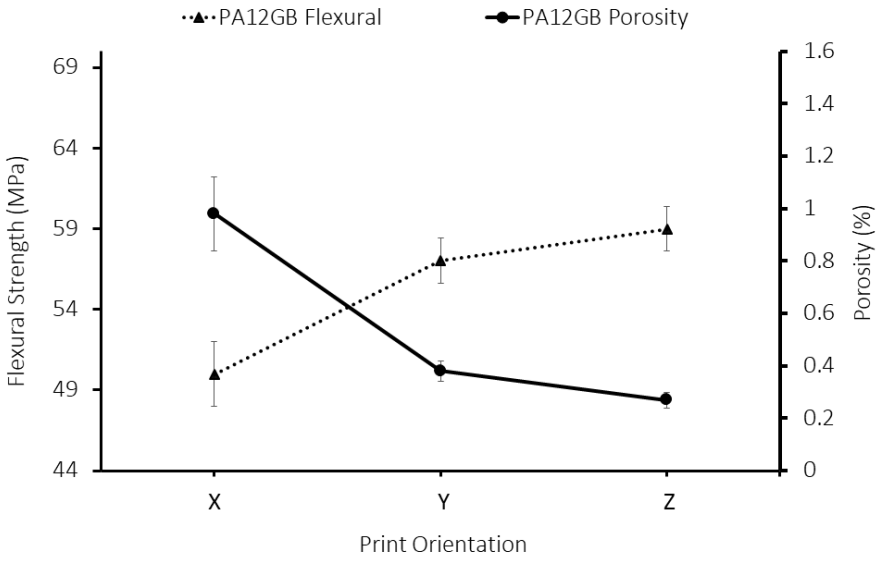


Figure 13: The flexural strength of PA12GB vs. part porosity

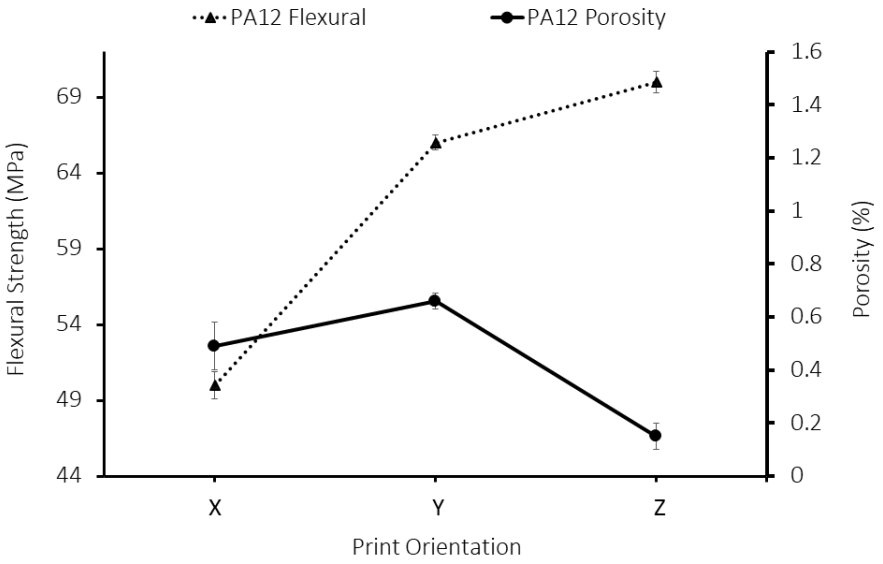


Figure 14: The flexural strength of PA12 vs. part porosity

## 4. Conclusions

This work has investigated the physical, chemical and mechanical properties of polyamide 12 glass bead parts, fabricated using a production scale, powder bed fusion process (HP Jet Fusion 3D 4200 printer). The results of which are compared with the polyamide 12 parts printed without any glass bead addition. As expected, both the polymer and composite exhibited similar chemical and thermal properties associated with the polyamide polymer.

The addition of 40% volume glass beads to the PA12 however, resulted in:

- An increase in the surface roughness of the PA12 composite part. For example, the Sa for the polymer was XX and that of the composite was YY μm.
- An 85% increase in tensile modulus, while the max tensile strength and elongation were both found to decrease. A similar trend was observed for the flexural strength and modulus. A factor influencing these results is likely to be the poor glass sphere – polymer matrix adhesion observed for the fracture surfaces by SEM.
- The incorporation of the glass spheres also resulted in a shift from a ductile failure mode obtained for the PA12 polymer, to a combination of both ductile and brittle failure modes for the composite.

The x-ray micro computed tomography results demonstrated that both the polymer and composite parts exhibited a largely homogeneous morphology, with porosities of less than 1%. Based on a literature comparison it was concluded that the mechanical properties of the PA12 composite, printing using the MJF process are comparable to those, printed using SLS. The influence of the part orientation on the flexural strength, as well as the porosity of the parts was evaluated. For both the polymer and PA12 composite, the flexural strength was found to increase in the following order, with print orientation X < Y < Z. In comparison to the PA12, the PA12 reinforced with glass beads exhibited enhanced stiffness and reduced overall strength.

**Acknowledgements:**

The authors would like to thank Henkel Ireland for supplying the printed parts and Dr. Saoirse Tracy, Director of the UCD X-ray CT facility at UCD Rosemount Experimental Research Station, for the use of the scanner. This work was supported under the I-Form Advanced Manufacturing Research Centre (16/RC/3872). The IR spectral acquisition was supported by the European Commission under the 7th Framework Programme (Grant agreement no:335508).

**References**


[1] B. Wendel, D. Rietzel, F. Kühnlein, R. Feulner, G. Hülder, E. Schmachtenberg, Additive Processing of Polymers, Macromolecular Materials and Engineering 293(10) (2008) 799-809.
[2] N. Standards, Additive manufacturing - General principles -Terminology (ISO/ASTM 52900:2015), I.S. EN ISO/ASTM 52900:2017, 2017.
[3] S. Yuan, F. Shen, C.K. Chua, K. Zhou, Polymeric composites for powder-based additive manufacturing: Materials and applications, Progress in Polymer Science (2018).
[4] A. Ellis, C.J. Noble, N. Hopkinson, High Speed Sintering: Assessing the influence of print density on microstructure and mechanical properties of nylon parts, Additive Manufacturing 1-4 (2014) 48-51.
[5] A.S. Kabalnov, J.T. WRIGHT, V. Kasperchik, Three-dimensional (3d) printing, Google Patents, 2016.
[6] H.J. O'Connor, A.N. Dickson, D.P. Dowling, Evaluation of the mechanical performance of polymer parts fabricated using a production scale multi jet fusion printing process, Additive Manufacturing 22 (2018) 381-387.
[7] R.D. Goodridge, C.J. Tuck, R.J.M. Hague, Laser sintering of polyamides and other polymers, Progress in Materials Science 57(2) (2012) 229-267.
[8] W. Zhu, C. Yan, Y. Shi, S. Wen, J. Liu, Q. Wei, Y. Shi, A novel method based on selective laser sintering for preparing high-performance carbon fibres/polyamide12/epoxy ternary composites, Sci Rep 6 (2016) 33780.
[9] G.M. Vasquez, C.E. Majewski, B. Haworth, N. Hopkinson, A targeted material selection process for polymers in laser sintering, Additive Manufacturing 1-4 (2014) 127-138.
[10] A. Salazar, A. Rico, J. Rodríguez, J. Segurado Escudero, R. Seltzer, F. Martin de la Escalera Cutillas, Monotonic loading and fatigue response of a bio-based polyamide PA11 and a petrol-based polyamide PA12 manufactured by selective laser sintering, European Polymer Journal 59 (2014) 36-45.
[11] J. Zhang, A. Adams, Understanding thermal aging of non-stabilized and stabilized polyamide 12 using 1H solid-state NMR, Polymer Degradation and Stability 134 (2016) 169-178.
[12] J.L. Leite, G.V. Salmoria, R.A. Paggi, C.H. Ahrens, A.S. Pouzada, Microstructural characterization and mechanical properties of functionally graded PA12/HDPE parts by selective laser sintering, International Journal of Advanced Manufacturing Technology (59) (2011) 583 - 591.
[13] S. Greiner, K. Wudy, L. Lanzl, D. Drummer, Selective laser sintering of polymer blends: Bulk properties and process behavior, Polymer Testing 64 (2017) 136-144.
[14] G.V. Salmoria, J.L. Leite, L.F. Vieira, A.T.N. Pires, C.R.M. Roesler, Mechanical properties of PA6/PA12 blend specimens prepared by selective laser sintering, Polymer Testing 31(3) (2012) 411-416.
[15] C. Yan, L. Hao, L. Xu, Y. Shi, Preparation, characterisation and processing of carbon fibre/polyamide-12 composites for selective laser sintering, Composites Science and Technology 71(16) (2011) 1834-1841.
[16] A. Mazzoli, G. Moriconi, M.G. Pauri, Characterization of an aluminum-filled polyamide powder for applications in selective laser sintering, Materials & Design 28(3) (2007) 993-1000.
[17] H. Chung, S. Das, Processing and properties of glass bead particulate-filled functionally graded Nylon-11 composites produced by selective laser sintering, Materials Science and Engineering: A 437(2) (2006) 226-234.
[18] Y. Wang, E. James, O.R. Ghita, Glass bead filled Polyetherketone (PEK) composite by High Temperature Laser Sintering (HT-LS), Materials & Design 83 (2015) 545-551.
[19] F. Qi, N. Chen, Q. Wang, Preparation of PA11/BaTiO3 nanocomposite powders with improved processability, dielectric and piezoelectric properties for use in selective laser sintering, Materials & Design 131 (2017) 135-143.
[20] Y. Chunze, S. Yusheng, Y. Jinsong, L. Jinhui, A Nanosilica/Nylon-12 Composite Powder for Selective Laser Sintering, Journal of Reinforced Plastics and Composites 28(23) (2008) 2889-2902.

[21] J. Kim, T.S. Creasy, Selective laser sintering characteristics of nylon 6/clay-reinforced nanocomposite, Polymer Testing 23(6) (2004) 629-636.
[22] S.R. Athreya, K. Kalaitzidou, S. Das, Processing and characterization of a carbon black-filled electrically conductive Nylon-12 nanocomposite produced by selective laser sintering, Materials Science and Engineering: A 527(10-11) (2010) 2637-2642.
[23] W. Shen, C.Y. Tang, C.P. Tsui, L.H. Peng, Effects of two damage mechanisms on effective elastic properties of particulate composites, Composites Science and Technology (62) (2002) 1397-1406.
[24] A.A. Mousa, D.T. Pham, S.P. Shwe, Pre-processing studies for selective laser sintering of glass beads-filled polyamide 12 composites, Int. J. Rapid Manufacturing 4(1) (2014) 28 - 48.
[25] J.Z.Liang, R.K.Y.Li, Mechanical Properties and Morphology of Glass Bead-Filled Polypropylene Composites, Polymer Composites 19(6) (1998) 698-703.
[26] R. Seltzer, F.M. de la Escalera, J. Segurado, Effect of water conditioning on the fracture behavior of PA12 composites processed by selective laser sintering, Materials Science and Engineering: A 528(22-23) (2011) 6927-6933.
[27] A.J. Cano, A. Salazar, J. Rodríguez, Effect of temperature on the fracture behavior of polyamide 12 and glass-filled polyamide 12 processed by selective laser sintering, Engineering Fracture Mechanics 203 (2018) 66-80.
[28] S. Negi, S. Dhiman, R.K. Sharma, Determining the effect of sintering conditions on mechanical properties of laser sintered glass filled polyamide parts using RSM, Measurement 68 (2015) 205-218.
[29] J. Xu, Y. Wu, L. Wang, J. Li, Y. Yang, Y. Tian, Z. Gong, P. Zhang, S. Nutt, S. Yin, Compressive properties of hollow lattice truss reinforced honeycombs (Honeytubes) by additive manufacturing: Patterning and tube alignment effects, Materials & Design 156 (2018) 446-457.
[30] HP 3D Printing materials, Hewlett packard, HP Indigo digital print, 2019.
[31] HP, HP 3D High Reusability PA 12 Glass Beads, 2019.
[32] HP, HP 3D High Reusability PA 12, 2019.
[33] B. Van Hooreweder, F. De Coninck, D. Moens, R. Boonen, P. Sas, Microstructural characterization of SLS-PA12 specimens under dynamic tension/compression excitation, Polymer Testing 29(3) (2010) 319-326.
[34] A. International, Standard Test Method for Tensile Properties of Plastics, ASTM D 638 - 02a (2002).
[35] A. International, Standard Test Methods for Flexural Properties of Unreinforced and Reinforced Plastics and Electrical Insulating Materials D 790, www.astm.org, 2003.
[36] S. Rhee, J.L. White, Crystal structure and morphology of biaxially oriented polyamide 12 films, Journal of Polymer Science Part B: Polymer Physics 40(12) (2002) 1189-1200.
[37] K. Inoue, S. Hoshino, Crystal structure of Nylon 12, Journal of Polymer Science : Polymer Physics Edition 11 (1973) 1077-1089.
[38] M.A. Czarnecki, P. Wu, H.W. Siesler, 2D FT-NIR and FT-IR correlation analysis of temperature-induced changed of nylon 12, Chemical Physics Letters 283 (1998) 326-332.
[39] P. Chen, M. Tang, W. Zhu, L. Yang, S. Wen, C. Yan, Z. Ji, H. Nan, Y. Shi, Systematical mechanism of Polyamide-12 aging and its micro-structural evolution during laser sintering, Polymer Testing 67 (2018) 370-379.
[40] D. Drummer, D. Rietzel, F. Kühnlein, Development of a characterization approach for the sintering behavior of new thermoplastics for selective laser sintering, Physics Procedia 5 (2010) 533-542.
[41] G. Craft, J. Nussbaum, N. Crane, J.P. Harmon, Impact of extended sintering times on mechanical properties in PA-12 parts produced by powderbed fusion processes, Additive Manufacturing 22 (2018) 800-806.
[42] A.A. Albarnawi, The effects of content and surface modification of filler on the mechanical properties of selective laser sintered polyamide12 composites, Jordan Journal of Mechanical and Industrial Engineering 8(5) (2014) 265-274.
[43] D. Rouholamin, N. Hopkinson, An investigation on the suitability of micro-computed tomography as a non-destructive technique to assess the morphology of laser sintered nylon 12 parts, Proceedings of the Institution of Mechanical Engineers, Part B: Journal of Engineering Manufacture 228(12) (2014) 1529-1542.

[44] S. Morales-Planas, J. Minguella-Canela, J. Lluma-Fuentes, J.A. Travieso-Rodriguez, A.A. Garcia-Granada, Multi Jet Fusion PA12 Manufacturing Parameters for Watertightness, Strength and Tolerances, Materials (Basel) 11(8) (2018).